Chemical Engineering Journal 507 (2025) 160101

Contents lists available at ScienceDirect

Chemical Engineering Journal

journal homepage: www.elsevier.com/locate/cej

Synergy of Ni single atoms and NiO nanoclusters in carbon nitride to create local charge polarization for enhanced CO_2 photoreduction

Lei Li [a,1], Xinyan Dai [b,1], Chao Cheng [a], Fang Chen [c,*], Saikh Mohammad Wabaidur [d], Wentao Wang [e,*], Yong Hu [f,*]

[a] Key Laboratory of the Ministry of Education for Advanced Catalysis Materials, Department of Chemistry, Zhejiang Normal University, Jinhua 321004, PR China
[b] Division of Natural and Applied Sciences, Duke Kunshan University, Kunshan 215316, PR China
[c] Hangzhou Institute of Advanced Studies, Zhejiang Normal University, Hangzhou 311231, PR China
[d] Chemistry Department, College of Science, King Saud University, Riyadh 11451, Saudi Arabia
[e] Guizhou Provincial Key Laboratory of Computational Nano-Material Science, Guizhou Education University, Guiyang 550018, PR China
[f] College of Chemistry and Materials Engineering, Zhejiang A&F University, Hangzhou 311300, PR China

ARTICLE INFO

Keywords:
Carbon nitrides
Ni single atoms
NiO nanoclusters
Local charge polarization
CO_2 photoreduction

ABSTRACT

Charge density distribution in metal single-atom (M-SA) catalysts is vital for charge transfer and molecular interactions with intermediate species. In this work, an ion-loading pyrolysis strategy has been developed to in-situ anchor Ni-SAs and NiO nanoclusters in holey g-C_3N_4 nanosheets for boosting photocatalytic reduction of CO_2 to CO through local charge polarization. The optimized photocatalyst achieves a high CO evolution rate of 42.55 μmol g^{-1} h^{-1} with nearly 100% selectivity. Both the spectroscopic and theoretical results reveal that NiO nanoclusters can alter the local electronic distribution by drawing electrons from adjacent Ni SAs through the g-C_3N_4 network and enhance the polarization of Ni–N bonds. Such electronic localization and polarization facilitate the separation of photogenerated charges via abundant Ni–N channels and tune the electronic structures of Ni-SA centers to optimize the adsorptions of intermediates in CO_2PR. This work opens a new avenue to construct advanced M-SA catalysts with metal oxide nanoclusters for high-efficiency photocatalytic CO_2 conversion.

1. Introduction

Carbon dioxide photoreduction (CO_2PR) enables solar energy conversion into fuels, holding great promise for advancing carbon neutrality [1,2]. Nonetheless, the efficiency of CO_2PR activity is hindered by the challenges of activating nonpolar CO_2 molecules and cleaving strong C=O double bonds with a high dissociation energy (~750 kJ mol^{-1}) [3,4]. Additionally, CO_2 reduction involves multiple steps of electron-coupled proton transfers [5,6], demanding appropriate electronic structure on active catalytic sites. Numerous photocatalysts have been developed to address such issues, encompassing metal-free and metal-containing materials (graphitic carbon nitride (g-C_3N_4) [7–9], metal–organic framework (MOF) [10–12], metal oxide [13,14], metal single-atoms (M-SAs) catalysts [15,16], and so on) with diverse nanoarchitectures.

M-SAs supported by g-C_3N_4 nanosheets (NSs) stand out from various catalysts due to their unique electronic properties. The substrates of two-dimensional g-C_3N_4 NSs inherit the advantages of bulk structures (distinctive electronic structures, chemical stability, ease of synthesis, and eco-friendliness) and exhibit plentiful active sites and rapid charge transfer [17–20]. Besides, orbital hybridizations between M-SAs with electronegative nitrogen atoms of g-C_3N_4 create metal–nitrogen (M−N) moieties and electronic metal-support interactions (EMSIs) for charge transfer [21–25]. However, sp^2 π-conjugated stacking architectures of g-C_3N_4 substrates induce relatively homogenous surface charge distribution [26]. Such high symmetries of charge distribution on M-SA catalysts manifest inferior adsorption/activation of nonpolar CO_2 molecules and directional charge separation/transfer [27,28].

Accordingly, some recent studies have proposed concepts of hetero-SAs catalysts pairing two different M-SAs (such as Cu/Co and Co/Ni) to induce localizations of positive or negative charges on various M-SA sites [29–31]. Another strategy to disrupt symmetry in charge distributions involves tailoring the coordination environments of M-SAs by introducing defects [32,33], electronegative heteroatoms [34–37], or

* Corresponding authors at: Hangzhou Institute of Advanced Studies, Zhejiang Normal University, Hangzhou 311231, PR China (F. Chen).
E-mail addresses: chenfang@zjnu.edu.cn (F. Chen), wtwang@gznc.edu.cn (W. Wang), yonghu@zafu.edu.cn (Y. Hu).
[1] These authors contributed equally to this work.

https://doi.org/10.1016/j.cej.2025.160101
Received 31 December 2024; Received in revised form 24 January 2025; Accepted 30 January 2025
Available online 8 February 2025

asymmetric coordination configurations [38,39]. The inhomogeneous charge distribution through these modification strategies enables adjustable d-band states of M-SAs and optimized adsorption/desorption strengths of reactive species. Furthermore, the polarized charge distribution can promote electron redistribution between g-C_3N_4 and M-SAs and strengthen EMSIs, thereby improving metal atomically dispersion and charge separation/transfer [29,34,40].

Motivated by these considerations, incorporating a secondary component represents an effective and straightforward approach to regulating the charge distribution of M-SA catalysts, thereby improving CO_2PR efficiency. In this work, we have developed an ion-loading pyrolysis route to in-situ co-loaded Ni-SAs and NiO nanoclusters onto g-C_3N_4 holey NSs (NiO/Ni_{SA}-CN HNSs) for efficient photocatalytic reduction of CO_2 to CO. Both experimental results and theoretical calculations reveal that NiO nanoclusters can accept electrons from Ni-SAs via Ni–N bridges and enhance the polarization of Ni–N bonds in Ni_{SA}-CN HNSs. The alterations of charge density endow NiO/Ni_{SA}-CN HNSs with expedited photoinduced charge separation and reduced energy barriers of CO_2PR–to–CO conversion. Therefore, NiO/Ni_{SA}-CN HNSs show an improved CO_2PR–to–CO activity of around 1.7 times higher than Ni_{SA}-CN HNSs. This work offers a local charge polarization approach to manipulate the electronic properties of M-SA sites and provides valuable insights into harnessing polarized engineering to develop high-efficiency CO_2PR photocatalysts.

2. Experimental section

2.1. Materials

Analytical-grade melamine, nickelous nitrate hexahydrate ($Ni(NO_3)_2{\cdot}6H_2O$), phosphoric acid, hydrochloric acid, absolute ethanol, glycerol, anhydrous sodium sulfate (Na_2SO_4). All the chemicals were purchased from Sinopharm Chemical Reagent Co., Ltd. (China) and directly used without further purification. Deionized water was used throughout the work.

2.2. Synthesis of NiO/Ni_{SA}-CN and pristine g-C_3N_4 (p-CN) HNSs

Initially, 500 mg of melamine, different molar percentage amounts of $Ni(NO_3)_2{\cdot}6H_2O$ to melamine (1, 2, 3, and 4 mol.%), and 600 mg of phosphorous acid were dissolved in 50 mL of deionized water at 80 °C with vigorous magnetic stirring for 1 h. The resulting mixture was then transferred into a Teflon-lined stainless-steel autoclave and maintained at 180 °C for 10 h. Subsequently, the sample was collected by centrifugation, washed with deionized water until neutrality, and dried at 60 °C for 12 h. The resulting sample was refluxed in a mixed aqueous solution containing 5 mL of glycerol and 15 mL of ethanol at 90 °C for 3 h. Afterward, the resulting product was collected by centrifugation, washed with ethanol, and dried at 60 °C in an oven. Finally, the powder samples were obtained by annealing the aforementioned powder at 500 °C for 2 h in a tube furnace with a heating rate of 2 °C min^{-1} under a hypoxic atmosphere. The obtained samples were marked as NiO/Ni_{SA}-CN–X (X = 1, 2, 3 and 4) HNSs. The p-CN HNSs were prepared using a similar method as NiO/Ni_{SA}-CN HNSs, except that without the addition of $Ni(NO_3)_2{\cdot}6H_2O$.

2.3. Synthesis of Ni_{SA}-CN HNSs

Ni_{SA}-CN HNSs were obtained through acid treatment to eliminate NiO nanoclusters, while maintaining the stable Ni-SAs sites according to the previous literature [41]. The as-prepared NiO/Ni_{SA}-CN–3 HNSs were dispersed in hydrochloric acid (0.5 M) and then vigorous magnetic stirring for 12 h. The obtained Ni_{SA}-CN HNSs were collected by centrifugation and washed with deionized water and absolute ethanol for several times, and then dried at 60 ℃ for 12 h.

Other experimental details including material characterizations, photophysical and (photo)electrochemical measurements, photocatalytic CO_2 reduction experiments, and theoretical calculations, can be found in the Appendix A. Supplementary data.

3. Results and discussion

3.1. Synthesis and structural characterization of the NiO/Ni_{SA}-CN HNSs

An ion-loading pyrolysis approach was adopted to co-anchor Ni-SAs and NiO nanoclusters into p-CN HNSs (Fig. 1a). The synthesis started with constructing Ni^{2+}-loaded supramolecular precursors, which were rich in functional groups of –NH_2 and –OH within tri-triazine layers, by the coordination-driven self-assembly of Ni^{2+} ions, melamine, and hydrolyzed cyanuric acid [15,21]. After inserting polar molecules of ethanol and glycerol into tri-triazine interlayers [19], the Ni^{2+}-loaded precursors were pyrolyzed at 500 °C in a hypoxic atmosphere to generate p-CN HNSs, Ni–N_6 moieties, and NiO nanoclusters concurrently. It is noted that electronegative nitrogen sites in p-CN HNSs can secure Ni-SAs and NiO nanoclusters through orbital hybridizations to promote charge transfer [15]. A series of NiO/Ni_{SA}-CN–X (X = 1 to 4) HNSs were prepared with increased additive amounts of Ni^{2+} ions. The control catalyst of p-CN HNSs was also prepared without adding Ni^{2+} ions. Acid etching to remove NiO nanoclusters in NiO/Ni_{SA}-CN–3 HNSs was employed to synthesize Ni_{SA}-CN HNSs for comparison.

Field emission scanning electron microscopy (FESEM) images reveal the layered microrod structure for the Ni^{2+}-loaded supramolecular precursors (**Fig. S1a**). The p-CN, Ni_{SA}-CN, and all NiO/Ni_{SA}-CN HNSs exhibit similar sheet-like structures featured by abundant macropores (Fig. 1b and S1b-f). Besides, nitrogen adsorption–desorption isotherms and Fourier-transform infrared spectra of studied catalysts show negligible variations in specific surface areas and molecular backbone configurations, respectively (**Figs. S2 and S3**). As presented in X-ray diffraction (XRD) results, all as-prepared samples display similar diffraction profiles of g-C_3N_4 [42], and no discernible NiO phase is detected in NiO/Ni_{SA}-CN HNSs (**Fig. S4**). These results reflect that similar porosity, molecular structure, and crystallinity of p-CN substrates are preserved in Ni_{SA}-CN and NiO/Ni_{SA}-CN HNSs.

Transmission electron microscopy (TEM) images of the NiO/Ni_{SA}-CN–3 HNSs reveal few-layered holey nanosheets of p-CN substrates with pore sizes ranging from tens to hundreds of nanometers (marked by red dash lines) (Fig. 1c and d). Besides, individual Ni-SA sites (circled in orange) are visualized in the aberration-corrected high-angle annular dark-field scanning TEM (AC HAADF-STEM) image with a sub-angstrom resolution (Fig. 1e). The numerous isolated Ni-SAs are distributed around NiO nanoclusters (circled in red) with an average size of about 0.8 nm (Fig. 1e). Moreover, the elemental mapping images of NiO/Ni_{SA}-CN–3 HNSs demonstrate uniform distributions for high abundances of C and N elements, alongside low concentrations of Ni and O elements (**Fig. S5**). The contents of Ni species in NiO/Ni_{SA}-CN HNSs were determined by atomic absorption spectrometry (AAS) (**Table S1**). Ni-SAs and NiO nanoclusters account for as high as 3.08 and 0.93 wt%, respectively, with the total Ni amount up to 3.81 wt%. Survey X-ray photoelectron spectroscopy (XPS) reveals the presence of C, N, Ni, and O elements in as-prepared catalysts (**Fig. S6a**). High-resolution XPS analyses were also investigated for NiO/Ni_{SA}-CN–3 HNSs. Contributions from C–N=C (398.66 eV), N–$(C)_3$ (399.68 eV), and –NH&NH_2 (400. 97 eV) are deconvoluted in the N 1s spectrum (Fig. 1f) [19]. The C 1s spectrum shows typical peaks of C–C (284.80 eV, adventitious carbon) and C–N=C (288.18 eV) [43], meanwhile, the lattice oxygen from NiO nanoclusters (530.15 eV) are identified in the O 1s spectrum (**Figs. S6b and c**) [44]. Additionally, the peak at 854.37 eV in the Ni $2p_{3/2}$ spectrum is located between those for Ni^{2+} ions (856.00 eV) and metallic Ni (853.10 eV) [45,46], indicating the coexistence of Ni^{2+} and partially reductive $Ni^{(2-\delta)+}$ species (Fig. 1g). The fractions of various elemental bonding configurations in Ni_{SA}-CN and NiO/Ni_{SA}-CN–3 HNSs measured by XPS as listed in **Table S2 and S3**. Compared to Ni_{SA}-CN HNSs, NiO/Ni_{SA}-

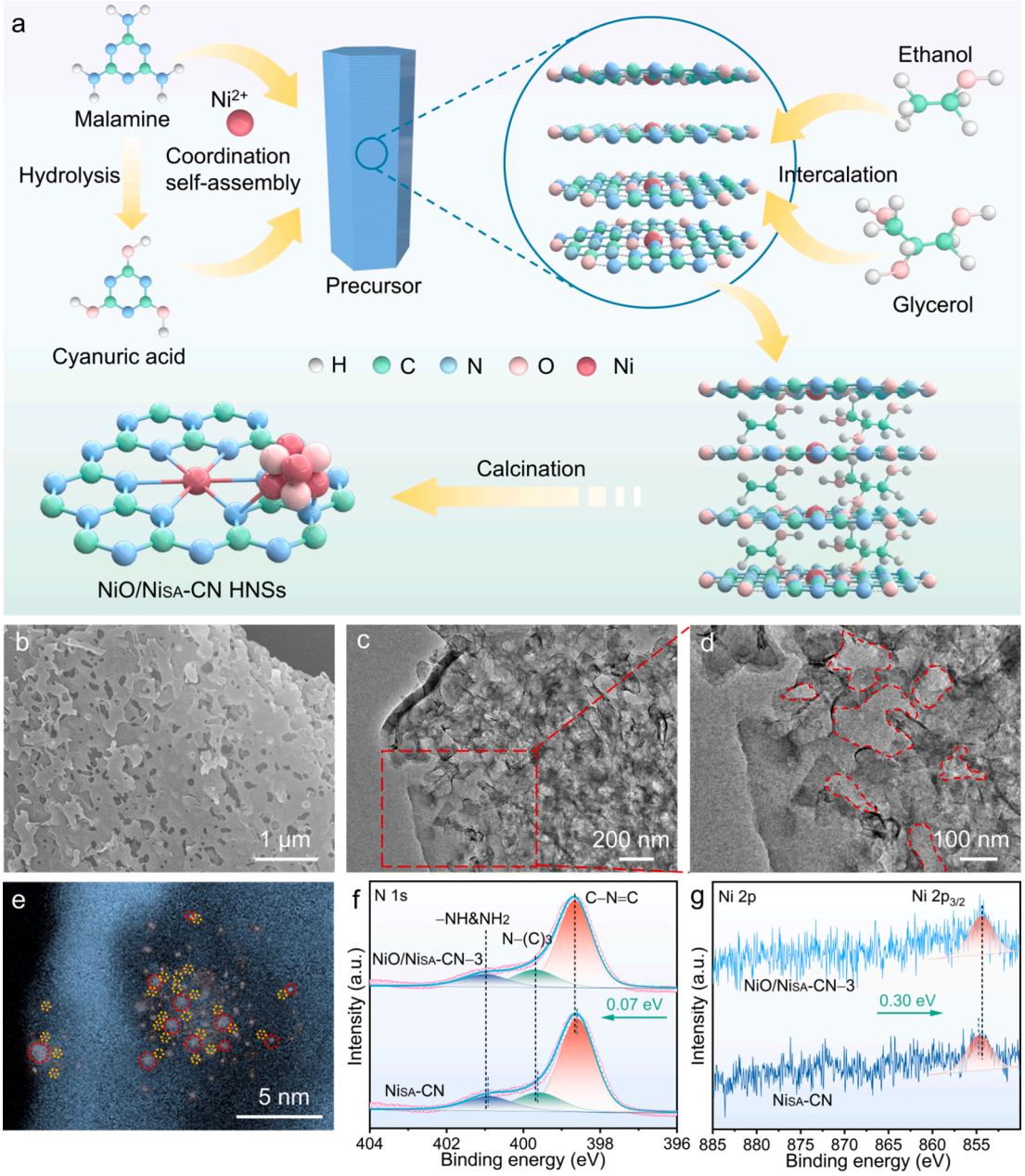

Fig. 1. (a) Schematic illustration of the synthetic process of the NiO/Ni_{SA}-CN HNSs. (b) FESEM, (c, d) TEM, (e) AC HAADF-STEM image of NiO/Ni_{SA}-CN–3 HNSs. The high-resolution XPS spectra of (f) N 1s and (g) Ni 2p for Ni_{SA}-CN, and NiO/Ni_{SA}-CN–3 HNSs.

CN–3 HNSs exhibit increased binding energies of C–N=C in C 1s and N 1s spectra, in contrast to the negative shift of Ni $2p_{3/2}$ peak. These results elucidate the role of NiO nanoclusters in altering the electronic distribution of Ni_{SA}-CN substrates. It seems that the electron density on Ni_{SA}-CN is reduced with more electrons transferring from Ni_{SA}-CN to NiO nanoclusters, thus resulting in partially reductive $Ni^{(2-\delta)+}$ species in NiO nanoclusters.

The valence states and coordination of Ni species in NiO/Ni_{SA}-CN–3 HNSs were elucidated by X-ray absorption near edge structure (XANES) and extended X-ray absorption fine structure (EXAFS). As shown in the Ni K-edge XANES curves, the absorption edge for NiO/Ni_{SA}-CN–3 HNSs is located between Ni foil and standard NiO (Fig. 2a**)**, in consistent with XPS results. It further confirms mixed oxidation states between 0 and +2 for Ni species, resulting from partially reductive NiO nanoclusters and isolated Ni-SAs. Fig. 2b presents Fourier-transformed k_3-weighted EXAFS spectra of NiO/Ni_{SA}-CN–3 HNSs. Two major well-scattered peaks at 1.53 and 2.55 Å in R-space are separately assigned to the first coordination shell of Ni–N in Ni_{SA}-CN substrates and the second shell of Ni–Ni in NiO nanoclusters, respectively [47]. Undetected Ni–Ni peak at 2.12 Å from Ni foil shows the absence of metallic Ni nanoparticles. The average Ni coordination numbers for Ni–N and Ni–Ni bonds are around 6.1 and 5.6, respectively (Fig. 2c, S7, and **Table S4**). It reflects the formation of thermally stable Ni–N_6 configurations and low-coordinated NiO nanoclusters with defect sites in NiO/Ni_{SA}-CN HNSs. Such structures are further supported by wavelet transform (WT) plots (Fig. 2d-f). Notably, the low coordination of NiO nanoclusters enables their strong interactions with nitrogen atoms in p-CN due to the formed Ni–N bonds.

3.2. *The polarization mechanism of electronic distributions*

According to coordination information, two theoretical models of Ni_{SA}-CN and NiO/Ni_{SA}-CN were constructed to reveal local electronic

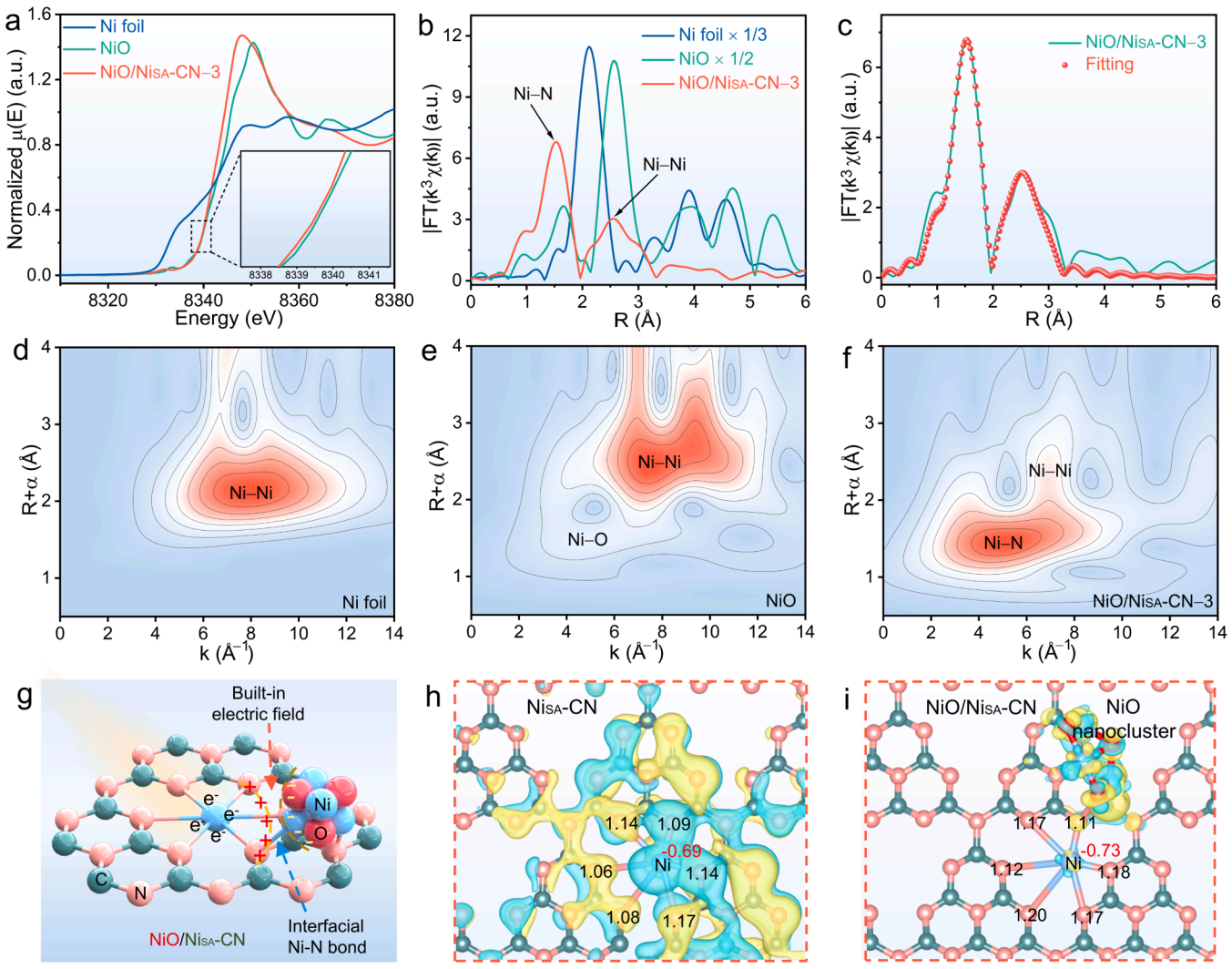

Fig. 2. (a) Normalized Ni K-edge XANES spectra (inset: the enlarged pre-edge absorption), (b) Fourier transform k_3-weighted EXAFS spectra of Ni foil, standard NiO, and NiO/Ni_{SA}-CN–3 HNSs. (c) EXAFS fitting curve of NiO/Ni_{SA}-CN–3 HNSs at R-space. WT-EXAFS analysis of (d)Ni foil, (e) standard NiO, and (f) NiO/Ni_{SA}-CN–3 HNSs. (g) Illustration of electronic interaction for a Ni-SA and NiO nanocluster to p-CN network through Ni–N bonds, in which photoexcited electron accumulation on a Ni-SA, and a built-in electric field directed from Ni_{SA}-CN towards the NiO nanocluster in NiO/Ni_{SA}-CN. Bader charge and differential charge distribution of (h) Ni_{SA}-CN, and (i) NiO/Ni_{SA}-CN. The isosurface value is set to 0.0003 e $Å^{-3}$. The yellow and cyan regions represent charge accumulation and depletion, respectively. The C, N, Ni, and O atoms are represented by grass green, brick red, baby blue, and red balls, respectively.

distribution by density functional theory (DFT) calculations. A Ni atom coordinate with six N atoms from C–N=C moieties in a single layer of g-C_3N_4 to construct the Ni_{SA}-CN model (**Fig. S8a**). Subsequently, Ni_{SA}-CN was decorated by a NiO nanocluster in adjacent sites of Ni-SAs to create NiO/Ni_{SA}-CN (**Fig. S8b**). Bader charge difference analysis reveals an electron accumulation on the NiO nanocluster and an electron depletion on the Ni_{SA}-CN substrate (**Fig. S9**), agreeing with XPS results. A total of 0.24 |e| charge is transferred from the Ni_{SA}-CN substrate to the NiO nanocluster. It means that NiO nanoclusters enable the polarization of electronic distributions by accepting electrons from Ni_{SA}-CN substrates. The negatively charged NiO nanoclusters and positively charged Ni_{SA}-CN substrates can create a built-in electric field at the interfacial region (Fig. 2g). Photogenerated holes accumulate in the NiO nanoclusters, while photoexcited electrons are transferred to the Ni–N_6 sites through Ni–N bridges. Therefore, it is supposed to facilitate photoexcited charge separation and transfer due to the synergy of Ni-SAs and NiO nanoclusters.

Moreover, N ligands of Ni–N_6 moieties for Ni_{SA}-CN have increased electron density by accepting an average of 1.11 |e|, in contrast to reduced electron density on Ni-SA centers with losing an average of 0.69 |e| (Fig. 2h). Nevertheless, those are 1.16 and 0.72 |e| for NiO/Ni_{SA}-CN, respectively (Fig. 2i). The difference in Bader charge transfer numbers increases from 1.80 to 1.88 |e| with the introduction of NiO nanoclusters, reflecting an increase in the polarity of the Ni–N bonds. Furthermore, the total electron density on Ni–N_6 site increases by 0.23 |e| for NiO/Ni_{SA}-CN in comparison to Ni_{SA}-CN, likely benefiting the adsorption and activation of electron-deficient CO_2 molecules. Experimental and theoretical analyses have demonstrated the presence of polarized electric fields between NiO nanoclusters and Ni_{SA}-CN substrates, along with those between N ligands and Ni-SA centers within Ni–N_6 sites.

3.3. *Photocatalytic CO_2 reduction performance*

To assess photoactivities of local polarized catalysts, visible light-driven CO_2PR was performed in a gas–solid reaction system. The gas–solid reaction system can allow the exposure of the catalyst surface to CO_2 atmosphere, and suppress the formation of H_2 from H_2O reduction [48,49]. All samples of p-CN, Ni_{SA}-CN, and NiO/Ni_{SA}-CN HNSs show CO evolution in 4 h with nearly 100% selectivity (Fig. 3a and S10).

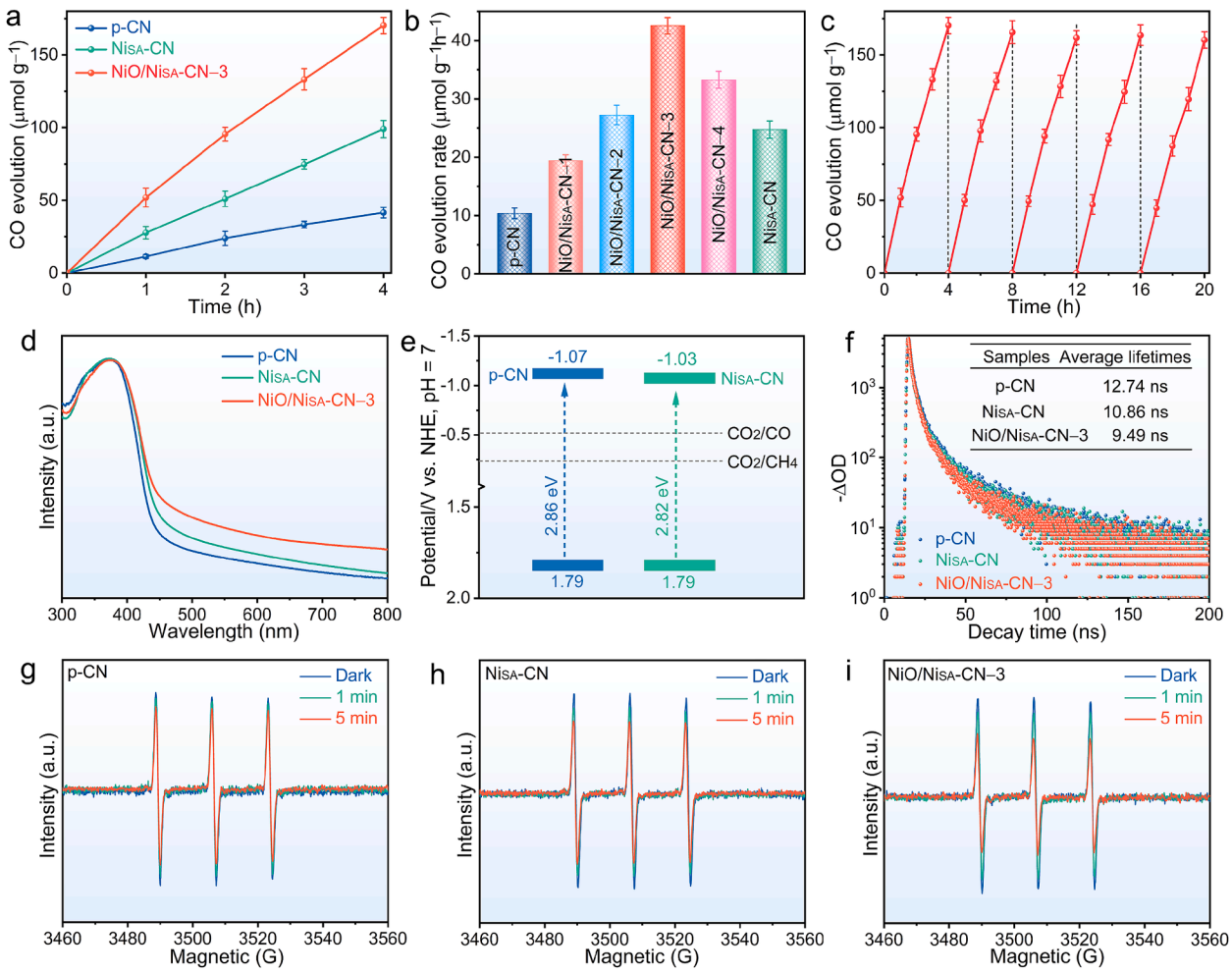

Fig. 3. (a) Time courses of CO evolution over p-CN, Ni_{SA}-CN, and NiO/Ni_{SA}-CN–3 HNSs. (b) Average CO gas evolution rates of as-prepared catalysts. (c) Cyclic stability test for CO_2PR on NiO/Ni_{SA}-CN–3 HNSs. Three repeated experiments were carried out for all the error estimates. (d) UV–vis DRS of p-CN, Ni_{SA}-CN, and NiO/Ni_{SA}-CN–3 HNSs. (e) electron energy bands of p-CN and Ni_{SA}-CN HNSs. (f) TRPL (inset of average lifetimes) of p-CN, Ni_{SA}-CN, and NiO/Ni_{SA}-CN–3 HNSs. In-situ ESR spectra of radical adduct signal labeled by TEMPO for electron capturing over (g) p-CN, (h) Ni_{SA}-CN, and (i) NiO/Ni_{SA}-CN–3 HNSs.

Neither other gaseous nor liquid products (such as H_2, CH_4, and CH_3OH) were detected (**Fig. S11**). Besides, NiO/Ni_{SA}-CN–3 HNSs with an optimal Ni amount exhibit the best CO evolution rate of 42.55 μmol g^{-1} h^{-1}, around 4.1 and 1.7 times higher than that of p-CN and Ni_{SA}-CN HNSs, respectively (Fig. 3b). NiO/Ni_{SA}-CN–3 HNSs exhibit the highest apparent quantum efficiency of 0.14% illuminated at 400 nm (**Fig. S12**, and equations S1 and S2). This superior activity surpasses the most advanced M-SA-modified g-C_3N_4 catalysts (**Table S5**). After five successive cycles over 20 h, NiO/Ni_{SA}-CN–3 HNSs display high photostability while preserving an original activity (Fig. 3c). The well-maintained morphology, crystal structures, and molecular backbone configuration of spent NiO/Ni_{SA}-CN–3 HNSs further evidence superior structural stabilities (**Fig. S13**). In control experiments, no products are observed in the dark or argon atmosphere (**Fig. S14**). Additionally, ^{13}C isotope experiments show a signal of $m/z = 29$ in mass spectra and a ^{13}CO signal in gas chromatography spectra (**Fig. S15**). These results validate that CO product is generated from CO_2 reactant gas instead of any organic impurities under visible light illumination.

3.4. Origins of photoactivity evolution

NiO nanoclusters play a significant role in polarizing local electronic distributions of Ni_{SA}-CN. It is supposed that microscopic changes can affect optical properties and efficiencies of charge separation and transfer. Electronic band structures were first investigated using ultraviolet−visible diffuse reflectance spectroscopy (UV–vis DRS) and Mott–Schottky (M−S) plots. Compared with p-CN HNSs, Ni_{SA}-CN HNSs show a slight increase in light absorption (Fig. 3d), which is reflected by the slightly narrower bandgap (2.82 eV) for the Ni_{SA}-CN HNSs (vs. p-CN, ca. 2.86 eV) (**Fig. S16a**). Additionally, the co-loading of Ni-SAs and NiO nanoclusters on p-CN HNSs enables NiO/Ni_{SA}-CN–3 HNSs sufficiently possess light-harvesting properties. The positive slopes of M−S plots reveal the n-type nature for as-parepared samples (**Figs. S16b-d**) [50]. Notably, the slope of M−S plots is reduced in an order of p-CN, Ni_{SA}-CN, and NiO/Ni_{SA}-CN–3 HNSs. This means that NiO nanoclusters endow Ni_{SA}-CN with improved charge carries density [51]. Note that the conduction band (E_{CB}) of n-type semiconductors is roughly equivalent to a flat band (E_{fb}) [52]. The E_{CBs} of p-CN and Ni_{SA}-CN HNSs are determined to be −1.07 and −1.03 V, respectively, relative to the normal hydrogen electrode (NHE) at pH = 7 (**Figs. S16b and c**). The negative location of E_{CB} compared to CO_2 reduction potential suggests the feasibility of CO_2PR over studied catalysts. Both p-CN and Ni_{SA}-CN HNSs exhibit the equal valence band (E_{VB}) of 1.79 V (vs. NHE, pH = 7) by a combined analysis of bandgaps and E_{CBs}. Thus, the band alignment and possible charge flow paths are illustrated in Fig. 3e and S17.

Photogenerated charge separation and transfer were then revealed by (photo)electrochemical measurements. The diminished photoluminescence (PL) emission intensity of NiO/Ni_{SA}-CN–3 HNSs shows the suppressed electron-hole recombination (**Fig. S18**) [53,54]. Besides, time-resolved PL (TRPL) decay curves can be fitted using a bi-

exponential model [55]. NiO/Ni_{SA}-CN–3 HNSs exhibit a lower average lifetime (τ) of 9.49 ns than control catalysts (12.74 ns for p-CN and 10.86 ns for Ni_{SA}-CN) (Fig. 3f). It is probably induced by additional nonradiative charge transfer pathways associated with available Ni–N channels [47,56]. Charge transfer efficiencies can be represented by electron rate constants (k_{et}), calculated by Equations (1) and (2):[47]

$$k_{et}(\text{p-CN}\rightarrow Ni_{SA}\text{-CN}) = 1/\tau(Ni_{SA}\text{-CN}) - 1/\tau(\text{p-CN}) \quad (1)$$

$$k_{et}(\text{p-CN}\rightarrow \text{NiO}/Ni_{SA}\text{-CN}) = 1/\tau(\text{NiO}/Ni_{SA}\text{-CN}) - 1/\tau(\text{p-CN}) \quad (2)$$

NiO/Ni_{SA}-CN–3 HNSs exhibit a higher k_{et} value than that of Ni_{SA}-CN HNSs (2.69×10^7 vs. 1.36×10^7), revealing improved charge transfer efficiency. Moreover, the photocurrent response of NiO/Ni_{SA}-CN–3 HNSs is increased compared to control catalysts due to its rapid charge separation (**Fig. S19**) [57]. The electrochemical impedance spectra (EIS) display the reduced arc radius of the Nyquist plots for NiO/Ni_{SA}-CN–3 HNSs, reflecting lowered interfacial charge transfer resistance (**Fig. S20**) [14]. The fitting results from EIS illustrate the NiO/Ni_{SA}-CN–3 HNSs possess the lowest charge transfer resistance (R_{ct}) among as-prepared samples (**Table S6**). Furthermore, the linear sweep voltammetry (LSV) curves in a CO_2-saturated sodium sulfate solution reveal a reduced overpotential for NiO/Ni_{SA}-CN–3 HNSs at the same current density (**Fig. S21a**). This is consistent with the corresponding Tafel slopes, indicating accelerated reaction kinetics associated with the CO_2 reduction process (**Fig. S21b**) [58]. It originates from high free electron density as indicated by small slopes of M−S plots and high energy densities of states across Fermi levels (**Figs. S16b-d and S22**).

The facilitated charge separation and transfer are supposed to boost photoinduced electron participated in surface reduction reactions. To confirm this hypothesis, the photoreduction of 2, 2, 6, 6-tetramethylpiperidinooxy (TEMPO) was conducted over various durations of light radiation (0 to 5 min). The residual amounts of TEMPO molecules were quantified by in-situ electron spin resonance (ESR) spectroscopy [59]. Compared to p-CN HNSs, Ni_{SA}-CN HNSs display low signal intensities, indicative of high TEMPO consumption rates (Fig. 3g and h). The TEMPO depletion is further accelerated over NiO/Ni_{SA}-CN–3 HNSs (Fig. 3i and S23). These results have verified that more photogenerated electrons are available to be captured by TEMPO after the introduction of Ni-SAs and NiO nanoclusters. The high availability of electrons results from a reduced charge migration barrier and expedited charge separation. Additionally, the electrochemical double-layer capacitance (C_{dl}) is tested by fitting cyclic voltammetry (CV) curves at different scanning rates (**Figs. S24a-c**). The C_{dl} value of NiO/Ni_{SA}-CN–3 HNSs (0.0956 mF cm^{-2}) is higher than that of p-CN (0.0656 mF cm^{-2}) and Ni_{SA}-CN HNSs (0.0764 mF cm^{-2}), demonstrating that Ni-SAs and NiO clusters endow NiO/Ni_{SA}-CN–3 HNSs more reactive sites to participate in the CO_2PR (**Fig. S24d**) [58].

Besides charge separation and transfer, the impact of NiO nanoclusters-assisted charge polarization on CO_2 adsorption was revealed by CO_2 adsorption isotherm curves (**Fig. S25**). The NiO/Ni_{SA}-CN–3 HNSs manifest an increased maximum CO_2 adsorption capacity (2.56 $cm^3\ g^{-1}$) compared to p-CN (1.20 $cm^3\ g^{-1}$) and Ni_{SA}-CN (1.87 $cm^3\ g^{-1}$). It is likely because more electron-deficient and nonpolar CO_2 molecules have high affinities with electron-enriched and polarized Ni–N_6 sites in the presence of NiO nanoclusters. The visible light-driven adsorbed CO_2 (*CO_2) activation and reduction were then monitored by in-situ diffuse reflection infrared Fourier transform spectroscopy (DRIFTS) measurements (Fig. 4 **and S26**). A couple of intermediates on studied catalysts are identified. They include monodentate carbonates (m-CO_3^{2-}, 1510 cm^{-1}), bidentate carbonates (b-CO_3^{2-}, 1333, 1549 and 1566 cm^{-1}), bicarbonates (HCO_3^-, 1667 cm^{-1}), •CO_2^- radicals (1271 and 1650 cm^{-1}), carboxylates (*COOH, 1710 cm^{-1}), and carbonyls (*CO, 2125 cm^{-1}) [60,61]. In contrast to p-CN HNSs with positive signal intensities, Ni_{SA}-CN and NiO/Ni_{SA}-CN–3 HNSs show negative values for most intermediates and positive values for *CO species. Compared to p-CN HNSs, adsorbed CO_2-derived species on Ni_{SA}-CN and NiO/Ni_{SA}-CN–3 HNSs are quickly consumed over light irradiation with low conversion barriers. The *CO_2 conversion on NiO/Ni_{SA}-CN–3 HNSs proceeds faster than Ni_{SA}-CN HNSs with more negative intensities, benefiting from highly polarized surface charge distribution.

3.5. Theoretical investigations of photocatalytic mechanism

A feasible reaction route is proposed according to DRIFT results.

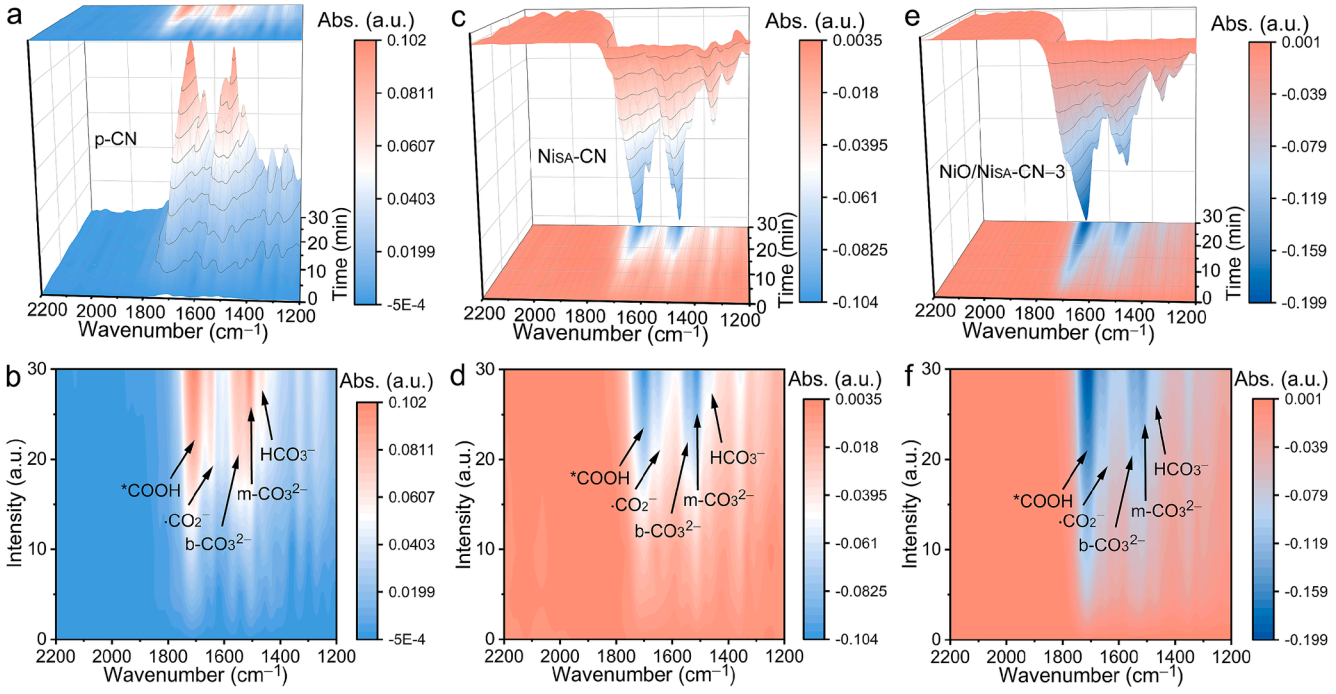

Fig. 4. (a, c, e) 3D color surface map and (b, d, f) the corresponding color contour map of in-situ DRIFTS of the as-prepared samples exposed to a mixture gas of He, CO_2, and H_2O with and without irradiation: (a, b) p-CN HNSs, (c, d) Ni_{SA}-CN HNSs, (e, f) NiO/Ni_{SA}-CN–3 HNSs.

After *CO_2 species are protonated and reduced to *COOH (*$CO_2 + H^+ + e^- \rightarrow$ *COOH), *COOH species are converted to *CO (*$COOH + H^+ + e^- \rightarrow$ *$CO + H_2O$). The final *CO desorption step results in the formation of CO product (*$CO \rightarrow * + CO$). Such reaction mechanism was further elucidated from Gibbs free energy diagrams for CO_2 reduction derived by DFT calculation (Fig. 5a and equations S3-S6). The energy barrier of *CO_2–to–*COOH on Ni_{SA}-CN is 1.01 eV, suggesting an endothermic process. Nevertheless, the decoration of NiO nanoclusters alters the step of *COOH formation to an exothermic process with a negative barrier of –0.43 eV. More importantly, the rate-determining step (RDS) for CO production lies in *CO desorption. Compared to Ni_{SA}-CN (1.51 eV), NiO/Ni_{SA}-CN show a reduced RDS barrier of 1.40 eV, consistent with their superior CO_2PR–to–CO activity. Besides, competing with CO evolution, CH_4 may be produced through the formation of formyl species (*CHO) from *CO. The reaction barrier for *CO–to–*CHO is higher than *CO–to–CO, indicating the high catalytic selectivity for both Ni_{SA}-CN and NiO/Ni_{SA}-CN, which is in agreement with the experimental result of nearly 100% CO product selectivity.

The Gibbs energy diagrams have shown that the reaction kinetics are dictated by the adsorption strength of *CO, which is closely correlated with the electronic structures of Ni-SA centers. As presented in the projected partial density of state (PDOS) analysis, the d-band center of NiO/Ni_{SA}-CN downshifts to –1.28 eV from –1.19 eV for Ni_{SA}-CN, in line with the reduced electron density on Ni-SA sites with NiO nanoclusters-assisted polarization (Fig. 2h and i). The negatively shifted d-band center away from the Fermi energy can induce more electrons to occupy antibonding orbitals of the Ni-SA center and *CO (Fig. 5b and c) [62]. Hence, the *CO adsorption is destabilized to facilitate CO_2PR–to–CO conversion.

4. Conclusion

In summary, a high-efficiency CO_2PR photocatalyst was achieved by in-situ anchoring NiO nanoclusters on the surroundings of Ni-SAs sites in p-CN HNSs substrates. Both the spectroscopic and theoretical results unveil that NiO nanoclusters can draw electrons from Ni_{SA}-CN substrates to promote the formation of the built-in electric field at the interfacial region, contributing to facilitated charge separation and transfer. Besides, NiO nanoclusters can destroy the delocalization of electrons from g-C_3N_4 network, localize electrons on neighboring Ni–N_6 active sites, and polarize Ni–N chemical bonds. The charge carrier density is increased due to such polarization effect. Moreover, the electron-enriched and polarized Ni–N_6 sites allow strong interactions with electron-deficient and nonpolar CO_2 molecules to improve CO_2 adsorption and activation capacities. Furthermore, the down-shift d-band center of Ni-SA centers with the presence of NiO nanoclusters weakens the *CO adsorption to promote CO production. As a result, the polarized NiO/Ni_{SA}-CN HNSs show an improved CO evolution rate up to 42.55 μmol g^{-1} h^{-1} with nearly 100% selectivity. This work presents in-depth insights into the engineering electronic properties of M-SAs photocatalysts.

CRediT authorship contribution statement

Lei Li: Writing – original draft, Validation, Data curation, Conceptualization. **Xinyan Dai:** Writing – original draft, Validation, Formal analysis, Data curation. **Chao Cheng:** Visualization, Software, Formal analysis. **Fang Chen:** Writing – review & editing, Validation, Formal analysis, Data curation. **Saikh Mohammad Wabaidur:** Writing – review & editing, Formal analysis. **Wentao Wang:** Validation, Software, Formal analysis, Data curation. **Yong Hu:** Writing – review & editing,

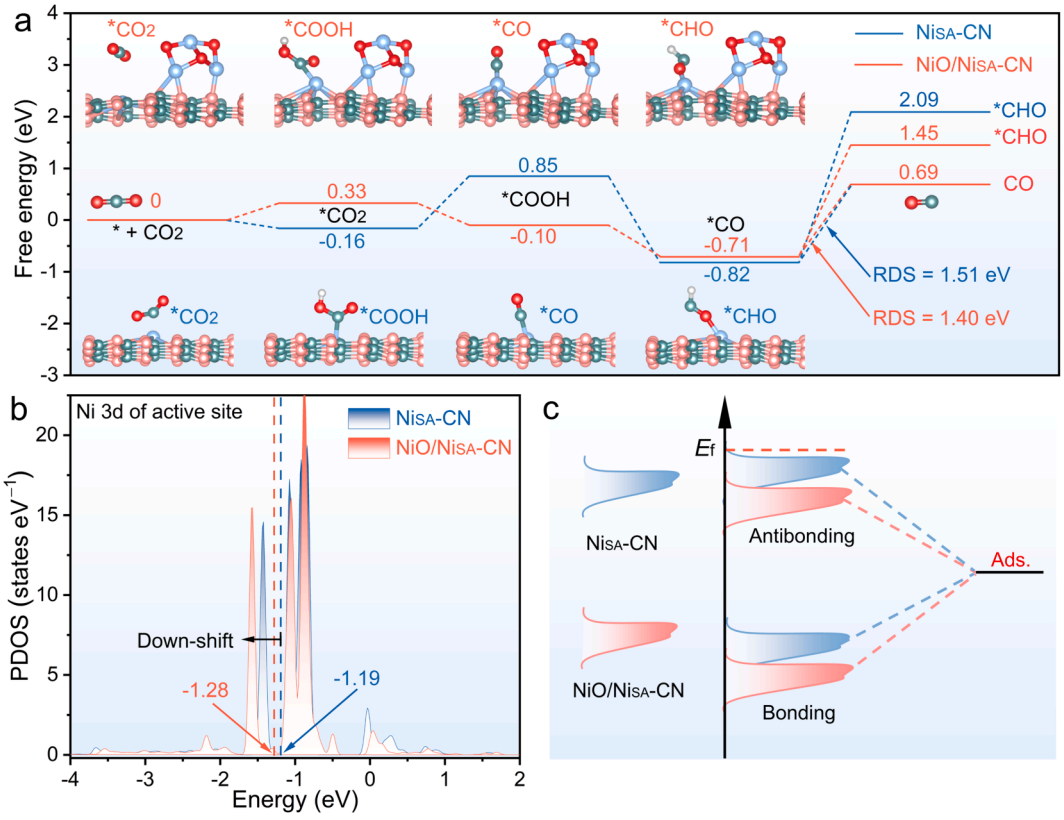

Fig. 5. (a) Gibbs free energy diagrams of CO_2 reduction on Ni_{SA}-CN and NiO/Ni_{SA}-CN. (b) PDOS projected on Ni 3d orbitals of single Ni active sites within Ni_{SA}-CN and NiO/Ni_{SA}-CN, with dash lines designating d-band centers. (c) Schematic illustration of bond formation between *CO adsorbate and isolated Ni centers in Ni_{SA}-CN (blue color) and NiO/Ni_{SA}-CN (brick red color). The ball-and-stick models of reaction intermediates are also presented, in which the C, N, Ni, O, and H atoms are represented by grass green, brick red, baby blue, red, and white balls, respectively.

Supervision, Project administration, Funding acquisition, Conceptualization.

Declaration of competing interest

The authors declare that they have no known competing financial interests or personal relationships that could have appeared to influence the work reported in this paper.

Acknowledgments

We appreciate the financial support from the National Natural Science Foundation of China (22272150 and 52262031), Zhejiang Provincial Ten Thousand Talent Program (2021R51009), Zhejiang Provincial Natural Science Foundation of China (LQ23B030006), and Guizhou provincial People's Government (Department of Education) Scholarship for Overseas Studies. Authors are grateful to the Researchers Supporting Project Number (RSP2025R448), King Saud University, Riyadh, Saudi Arabia. This work is carried out at Shanxi Supercomputing Center of China, and the calculations are performed on TianHe-2. This research is also supported by the advanced computing resources provided by the Supercomputing Center of the USTC.

Appendix A. Supplementary data

Supplementary data to this article can be found online at https://doi.org/10.1016/j.cej.2025.160101.

Data availability

The authors do not have permission to share data.

References

[1] H. Rao, L.C. Schmidt, J. Bonin, M. Robert, Visible-light-driven methane formation from CO_2 with a molecular iron catalyst, Nature 548 (2017) 74–77, https://doi.org/10.1038/nature23016.
[2] C. Wang, Y. Zhao, C. Cheng, Q. Li, C. Guo, Y. Hu, S-scheme heterojunction photocatalysts: Mechanism, challenges and opportunities, Coord. Chem. Rev. 521 (2024) 216177, https://doi.org/10.1016/j.ccr.2024.216177.
[3] X. Li, Y. Sun, J. Xu, Y. Shao, J. Wu, X. Xu, Y. Pan, H. Ju, J. Zhu, Y. Xie, Selective visible-light-driven photocatalytic CO_2 reduction to CH_4 mediated by atomically thin $CuIn_5S_8$ layers, Nat. Energy 4 (2019) 690–699, https://doi.org/10.1038/s41560-019-0431-1.
[4] J. Li, X. Liu, X. Wu, Z. Liu, Z. Zhao, Y. Liu, S. Dou, Y. Xiao, Selective CO_2 photoreduction into CH_4 triggered by the synergy between oxygen vacancy and Ru substitution under near-infrared light irradiation, Adv. Sci. 11 (2024) 2405668, https://doi.org/10.1002/advs.202405668.
[5] X. Shi, Y. Huang, Y. Bo, D. Duan, Z. Wang, J. Cao, G. Zhu, W. Ho, L. Wang, T. Huang, Y. Xiong, Highly selective photocatalytic CO_2 methanation with water vapor on single-atom platinum-decorated defective carbon nitride, Angew. Chem. Int. Ed. 61 (2022) e202203063.
[6] C. Cheng, H. Xu, M. Ni, C. Guo, Y. Zhao, Y. Hu, Interfacial electron interactions governed photoactivity and selectivity evolution of carbon dioxide photoreduction with spinel cobalt oxide based hollow hetero-nanocubes, Appl. Catal. B-Environ. Energy 345 (2024) 123705, https://doi.org/10.1016/j.apcatb.2024.123705.
[7] H. Dong, L. Tong, P. Zhang, D. Zhu, J. Jiang, C. Li, Built-in electric field intensified by photothermoelectric effect drives charge separation over Z-scheme 3D/2D In_2Se_3/PCN heterojunction for high-efficiency photocatalytic CO_2 reduction, J. Mater. Sci. Technol. 179 (2024) 251–261, https://doi.org/10.1016/j.jmst.2023.10.012.
[8] C. Li, P. Zhang, F. Gu, L. Tong, J. Jiang, Y. Zuo, H. Dong, Atomically dispersed Au confined by oxygen vacancies in Au-θ-Al_2O_3/Au/PCN hybrid for boosting photocatalytic CO_2 reduction driven by multiple built-in electric fields, Chem. Eng. J. 476 (2023) 146514, https://doi.org/10.1016/j.cej.2023.146514.
[9] M.Y. Akram, T. Ashraf, L. Tong, X. Yin, H. Dong, H. Lu, Architecting high-performance photocatalysts: A review of modified 2D/2D graphene/g-C_3N_4 heterostructures, J. Environ. Chem. Eng. 12 (2024) 113415, https://doi.org/10.1016/j.jece.2024.113415.
[10] C. Li, J. Wang, L. Tong, Y. Wang, P. Zhang, M. Zhu, H. Dong, Recent progress and challenges of photocatalytic CO_2 conversion into value-added multi-carbon products, Coord. Chem. Rev. 502 (2024) 215623, https://doi.org/10.1016/j.ccr.2023.215623.
[11] J. Li, J. Jia, D. Wang, H. Dong, M. Zhu, Recent research progress of MOFs-based heterostructures for photocatalytic hydrogen evolution, Chem. Eng. J. 498 (2024) 155194, https://doi.org/10.1016/j.cej.2024.155194.
[12] P. Zhang, H. Cheng, F. Gu, S. Hong, H. Dong, C. Li, Progress on iron-series metal-organic frameworks materials towards electrocatalytic hydrogen evolution reaction, Surf. Interfaces 42 (2023) 103368, https://doi.org/10.1016/j.surfin.2023.103368.
[13] L. Li, H. Liu, T. Li, F. Chen, W. Wang, J. Ning, Y. Hu, Modulating the moderate d-band center of indium in $InVO_4$ nanobelts by synergizing MnO and oxygen vacancies for high-efficiency CO_2 photoreduction, Small 20 (2024) 2404909, https://doi.org/10.1002/smll.202404909.
[14] M. Ni, Y. Zhu, C. Guo, D.L. Chen, J. Ning, Y. Zhong, Y. Hu, Efficient visible-light-driven CO_2 methanation with self-regenerated oxygen vacancies in Co_3O_4/$NiCo_2O_4$ hetero-nanocages: Vacancy-mediated selective photocatalysis, ACS Catal. 14 (2023) 2502–2512, https://doi.org/10.1021/acscatal.2c05577.
[15] L. Li, X. Dai, M. Lu, C. Guo, S.M. Wabaidur, X.L. Wu, Z. Lou, Y. Zhong, Y. Hu, Electron-enriched single-Pd-sites on g-C_3N_4 nanosheets achieved by in-situ anchoring twinned Pd nanoparticles for efficient CO_2 photoreduction, Adv. Powder Mater. 3 (2024) 100170, https://doi.org/10.1016/j.apmate.2024.100170.
[16] Z. Xie, L. Li, S. Gong, S. Xu, H. Luo, D. Li, H. Chen, M. Chen, K. Liu, W. Shi, D. Xu, Y. Lei, Clustering-resistant Cu single atoms on porous Au nanoparticles supported by TiO_2 for sustainable photoconversion of CO_2 into CH_4, Angew. Chem. Int. Ed. 63 (2024) e202410250.
[17] X. Wang, K. Maeda, A. Thomas, K. Takanabe, G. Xin, J.M. Carlsson, K. Domen, M. Antonietti, A metal-free polymeric photocatalyst for hydrogen production from water under visible light, Nat. Mater. 8 (2009) 76–80, https://doi.org/10.1038/nmat2317.
[18] C. Ding, X. Lu, B. Tao, L. Yang, X. Xu, L. Tang, H. Chi, Y. Yang, D.M. Meira, L. Wang, X. Zhu, S. Li, Y. Zhou, Z. Zou, Interlayer spacing regulation by single-atom indium$^{\delta+}$–N_4 on carbon nitride for boosting CO_2/CO photo-conversion, Adv. Funct. Mater. 33 (2023) 2302824, https://doi.org/10.1002/adfm.202302824.
[19] Y. Xiao, G. Tian, W. Li, Y. Xie, B. Jiang, C. Tian, D. Zhao, H. Fu, Molecule self-assembly synthesis of porous few-layer carbon nitride for highly efficient photoredox catalysis, J. Am. Chem. Soc. 141 (2019) 2508–2515, https://doi.org/10.1021/jacs.8b12428.
[20] X. Zhao, Q. Liu, X. Li, H. Ji, Z. Shen, Two-dimensional g-C_3N_4 nanosheets-based photo-catalysts for typical sustainable processes, Chin. Chem. Lett. 34 (2023) 108306, https://doi.org/10.1016/j.cclet.2023.108306.
[21] X. Xiao, Y. Gao, L. Zhang, J. Zhang, Q. Zhang, Q. Li, H. Bao, J. Zhou, S. Miao, N. Chen, J. Wang, B. Jiang, C. Tian, H. Fu, A promoted charge separation/transfer system from Cu single atoms and C_3N_4 layers for efficient photocatalysis, Adv. Mater. 32 (2020) 2003082, https://doi.org/10.1002/adma.202003082.
[22] M. Qian, X.L. Wu, M. Lu, L. Huang, W. Li, H. Lin, J. Chen, S. Wang, X. Duan, Modulation of charge trapping by island-like single-atom cobalt catalyst for enhanced photo-fenton-like reaction, Adv. Funct. Mater. 33 (2023) 2370072, https://doi.org/10.1002/adfm.202370072.
[23] P. Zhou, M. Luo, S. Guo, Optimizing the semiconductor–metal-single-atom interaction for photocatalytic reactivity, Nat. Rev. Chem. 6 (2022) 823–838, https://doi.org/10.1038/s41570-022-00434-1.
[24] H. Shi, H. Wang, Y. Zhou, J. Li, P. Zhai, X. Li, G.G. Gurzadyan, J. Hou, H. Yang, X. Guo, Atomically dispersed indium-copper dual-metal active sites promoting C−C coupling for CO_2 photoreduction to ethanol, Angew. Chem. Int. Ed. 61 (2022) e202208904.
[25] H. Ou, S. Ning, P. Zhu, S. Chen, A. Han, Q. Kang, Z. Hu, J. Ye, D. Wang, Y. Li, Carbon nitride photocatalysts with integrated oxidation and reduction atomic active centers for improved CO_2 conversion, Angew. Chem. Int. Ed. 61 (2022) e202206579.
[26] S. Hu, P. Qiao, X. Liang, G. Ba, X. Zu, H. Hu, J. Ye, D. Wang, Single-atom Pt–N_4 active sites anchored on porous C_3N_4 nanosheet for boosting the photocatalytic CO_2 reduction with nearly 100% CO selectivity, Appl. Catal. B-Environ. Energy 346 (2024) 123737, https://doi.org/10.1016/j.apcatb.2024.123737.
[27] Y. Wang, Q. Wang, J. Wu, X. Zhao, Y. Xiong, F. Luo, Y. Lei, Asymmetric atomic sites make different: Recent progress in electrocatalytic CO_2 reduction, Nano Energy 103 (2022) 107815, https://doi.org/10.1016/j.nanoen.2022.107815.
[28] J. Di, C. Chen, Y. Wu, H. Chen, J. Xiong, R. Long, S. Li, L. Song, W. Jiang, Z. Liu, Asymmetric electron redistribution in niobic-oxygen vacancy associates to tune noncovalent interaction in CO_2 photoreduction, Adv. Mater. 36 (2024) 2401914, https://doi.org/10.1002/adma.202401914.
[29] X. Zhao, F. Wang, X.-P. Kong, R. Fang, Y. Li, Dual-metal hetero-single-atoms with different coordination for efficient synergistic catalysis, J. Am. Chem. Soc. 143 (2021) 16068–16077, https://doi.org/10.1021/jacs.1c06349.
[30] Y. Zhu, J. Sokolowski, X. Song, Y. He, Y. Mei, G. Wu, Engineering local coordination environments of atomically dispersed and heteroatom-coordinated single metal site electrocatalysts for clean energy-conversion, Adv. Energy Mater. 10 (2020) 1902844, https://doi.org/10.1002/aenm.201902844.
[31] N. Song, J. Jiang, S. Hong, Y. Wang, C. Li, H. Dong, State-of-the-art advancements in single atom electrocatalysts originating from MOFs for electrochemical energy conversion, Chinese, J. Catal. 59 (2024) 38–81, https://doi.org/10.1016/S1872-2067(23)64622-4.
[32] D. Mao, T. Li, X. Lu, T. Guo, H. He, H. Fu, Z. Liu, S. Zheng, C. Sun, Z. Xu, Z. Jiang, X. Qu, Regulating local polarization in hollow multi-shelled nanospheres for efficient atomic site activation towards selective aerobic oxidation of aromatic alcohols, Appl. Catal. B-Environ. Energy 359 (2024) 124481, https://doi.org/10.1016/j.apcatb.2024.124481.
[33] P. Zhang, S. Hong, N. Song, Z. Han, F. Ge, G. Dai, H. Dong, C. Li, Alloy as advanced catalysts for electrocatalysis: From materials design to applications, Chin. Chem. Lett. 35 (2024) 109073, https://doi.org/10.1016/j.cclet.2023.109073.
[34] F. Cao, X. Zhang, Z. Jin, J. Zhang, Z. Tian, D. Kong, Y. Li, Y. Li, L. Zhi, Electronegativity matching of asymmetrically coordinated single-atom catalysts for

high-performance lithium–sulfur batteries, Adv. Energy Mater. 14 (2024) 2303893, https://doi.org/10.1002/aenm.202303893.
[35] K. Yuan, D. Lützenkirchen-Hecht, L. Li, L. Shuai, Y. Li, R. Cao, M. Qiu, X. Zhuang, M.K.H. Leung, Y. Chen, U. Scherf, Boosting oxygen reduction of single iron active sites via geometric and electronic engineering: Nitrogen and phosphorus dual coordination, J. Am. Chem. Soc. 142 (2020) 2404–2412, https://doi.org/10.1021/jacs.9b11852.
[36] S. Guo, P. Yuan, J. Zhang, P. Jin, H. Sun, K. Lei, X. Pang, Q. Xu, F. Cheng, Atomic-scaled cobalt encapsulated in P, N-doped carbon sheaths over carbon nanotubes for enhanced oxygen reduction electrocatalysis under acidic and alkaline media, Chem. Commun. 53 (2017) 9862–9865, https://doi.org/10.1039/C7CC05476A.
[37] Y. Guo, P. Yuan, J. Zhang, Y. Hu, I.S. Amiinu, X. Wang, J. Zhou, H. Xia, Z. Song, Q. Xu, S. Mu, Carbon nanosheets containing discrete Co-N_x-B_y-C active sites for efficient oxygen electrocatalysis and rechargeable Zn–air batteries, ACS Nano 12 (2018) 1894–1901, https://doi.org/10.1021/acsnano.7b08721.
[38] Y. Duan, Y. Wang, W. Zhang, J. Zhang, C. Ban, D. Yu, K. Zhou, J. Tang, X. Zhang, X. Han, L. Gan, X. Tao, X. Zhou, Simultaneous CO_2 and H_2O activation via integrated Cu single atom and N vacancy dual-site for enhanced CO photoproduction, Adv. Funct. Mater. 33 (2023) 2301729, https://doi.org/10.1002/adfm.202301729.
[39] S. Hu, P. Qiao, X. Yi, Y. Lei, H. Hu, J. Ye, D. Wang, Selective photocatalytic reduction of CO_2 to CO mediated by silver single atoms anchored on tubular carbon nitride, Angew. Chem. Int. Ed. 62 (2023) e202304585.
[40] B.K.Y. Ng, Z.J. Zhou, T.T. Liu, T. Yoskamtorn, G. Li, T.S. Wu, Y.L. Soo, X.P. Wu, S.C. E. Tsang, Photo-induced active Lewis acid–base pairs in a metal–organic framework for H_2 activation, J. Am. Chem. Soc. 145 (2023) 19312–19320, https://doi.org/10.1021/jacs.3c05244.
[41] Y. Li, S. Wang, X. s. Wang, Y. He, Q. Wang, Y. Li, M. Li, G. Yang, J. Yi, H. Lin, D. Huang, L. Li, H. Chen, J. Ye, Facile top-down strategy for direct metal atomization and coordination achieving a high turnover number in CO_2 photoreduction, J. Am. Chem. Soc. 142 (2020) 19259-19267, https://doi.org/10.1021/jacs.0c09060.
[42] L. Wang, D. Chen, S. Miao, F. Chen, C. Guo, P. Ye, J. Ning, Y. Zhong, Y. Hu, Nitric acid-assisted growth of $InVO_4$ nanobelts on protonated ultrathin C_3N_4 nanosheets as an S-scheme photocatalyst with tunable oxygen vacancies for boosting CO_2 conversion, Chem. Eng. J. 434 (2022) 133867, https://doi.org/10.1016/j.cej.2021.133867.
[43] X. Wu, R. Zhong, X. Lv, Z. Hu, D. Xia, C. Li, B. Song, S. Liu, Modulating g-C_3N_4-based van der Waals heterostructures with spatially separated reductive centers for tandem photocatalytic CO_2 methanation, Appl. Catal. B-Environ. 330 (2023) 122666, https://doi.org/10.1016/j.apcatb.2023.122666.
[44] J.H. Lee, Y.W. Noh, I.S. Jin, S.H. Park, J.W. Jung, Facile surface engineering of nickel oxide thin film for enhanced power conversion efficiency of planar heterojunction perovskite solar cells, ACS Sustainable Chem. Eng. 7 (2019) 15495–15503, https://doi.org/10.1021/acssuschemeng.9b03148.
[45] Y. Tang, Y. Wei, Z. Wang, S. Zhang, Y. Li, L. Nguyen, Y. Li, Y. Zhou, W. Shen, F. F. Tao, P. Hu, Synergy of single-atom Ni_1 and Ru_1 sites on CeO_2 for dry reforming of CH_4, J. Am. Chem. Soc. 141 (2019) 7283–7293, https://doi.org/10.1021/jacs.8b10910.
[46] L. Zhang, D. Liu, Z. Muhammad, F. Wan, W. Xie, Y. Wang, L. Song, Z. Niu, J. Chen, Single nickel atoms on nitrogen-doped graphene enabling enhanced kinetics of lithium–sulfur batteries, Adv. Mater. 31 (2019) 1903955, https://doi.org/10.1002/adma.201903955.
[47] L. Cheng, H. Yin, C. Cai, J. Fan, Q. Xiang, Single Ni atoms anchored on porous few-layer g-C_3N_4 for photocatalytic CO_2 reduction: The role of edge confinement, Small 16 (2020) e2002411.
[48] J. Fu, K. Jiang, X. Qiu, J. Yu, M. Liu, Product selectivity of photocatalytic CO_2 reduction reactions, Mater. Today 32 (2020) 222–243, https://doi.org/10.1016/j.mattod.2019.06.009.
[49] S. Xie, Y. Wang, Q. Zhang, W. Deng, Y. Wang, MgO- and Pt-promoted TiO_2 as an efficient photocatalyst for the preferential reduction of carbon dioxide in the presence of water, ACS Catal. 4 (2014) 3644–3653, https://doi.org/10.1021/cs500648p.
[50] L. Li, H. Liu, C. Cheng, X. Dai, F. Chen, J. Ning, W. Wang, Y. Hu, Photochemical tuning of tricoordinated nitrogen deficiency in carbon nitride to create delocalized π electron clouds for efficient CO_2 photoreduction, ACS Catal. 14 (2024) 10204–10213, https://doi.org/10.1021/acscatal.4c01636.
[51] Z. Zhang, L. Zhang, M.N. Hedhili, H. Zhang, P. Wang, Plasmonic gold nanocrystals coupled with photonic crystal seamlessly on TiO_2 nanotube photoelectrodes for efficient visible light photoelectrochemical water splitting, Nano Lett. 13 (2013) 14–20, https://doi.org/10.1021/nl3029202.
[52] T.W. Kim, K.S. Choi, Nanoporous $BiVO_4$ photoanodes with dual-layer oxygen evolution catalysts for solar water splitting, Science 343 (2014) 990–994, https://doi.org/10.1126/science.1246913.
[53] Y. Hu, S. Zhang, Z. Zhang, H. Zhou, B. Li, Z. Sun, X. Hu, W. Yang, X. Li, Y. Wang, S. Liu, D. Wang, J. Lin, W. Chen, S. Wang, Enhancing photocatalytic-transfer semi-hydrogenation of alkynes over Pd/C_3N_4 through dual regulation of nitrogen defects and the Mott–Schottky effect, Adv. Mater. 35 (2023) 202304130, https://doi.org/10.1002/adma.202304130.
[54] L. Li, X. Dai, D.L. Chen, Y. Zeng, Y. Hu, X.W. Lou, Steering catalytic activity and selectivity of CO_2 photoreduction to syngas with hydroxy-rich $Cu_2S@R_{OH}$-$NiCo_2O_3$ double-shelled nanoboxes, Angew. Chem. Int. Ed. 61 (2022) e202205839.
[55] P. Xiao, J. Lou, H. Zhang, W. Song, X.L. Wu, H. Lin, J. Chen, S. Liu, X. Wang, Enhanced visible-light-driven photocatalysis from WS_2 quantum dots coupled to BiOCl nanosheets: Synergistic effect and mechanism insight, Catal, Sci. Technol. 8 (2018) 201–209, https://doi.org/10.1039/C7CY01784G.
[56] K. Sun, J. Shen, Q. Liu, H. Tang, M. Zhang, S. Zulfiqar, C. Lei, Synergistic effect of Co(II)-hole and Pt-electron cocatalysts for enhanced photocatalytic hydrogen evolution performance of P-doped g-C_3N_4, Chinese, J. Catal. 41 (2020) 72–81, https://doi.org/10.1016/S1872-2067(19)63430-3.
[57] Y. Chai, Y. Kong, M. Lin, W. Lin, J. Shen, J. Long, R. Yuan, W. Dai, X. Wang, Z. Zhang, Metal to non-metal sites of metallic sulfides switching products from CO to CH_4 for photocatalytic CO_2 reduction, Nat. Commun. 14 (2023) 6168, https://doi.org/10.1038/s41467-023-41943-x.
[58] Z. Xu, J. Chen, T. Zhang, H. Lu, L. Yan, J. Ning, Y. Hu, Enhancing efficiency and durability of alkaline Zn-Co/air hybrid batteries with self-reconstructed Co/Co_2P heterojunctions, Adv. Energy Mater. 2402839 (2024), https://doi.org/10.1002/aenm.202402839.
[59] S. Li, N. Huber, W. Huang, W. Wei, K. Landfester, C.T.J. Ferguson, Y. Zhao, K.A. I. Zhang, Triazine frameworks for the photocatalytic selective oxidation of toluene, Angew. Chem. Int. Ed. 63 (2024) e202400101.
[60] X. Shi, X. a. Dong, Y. He, P. Yan, S. Zhang, F. Dong, Photoswitchable chlorine vacancies in ultrathin $Bi_4O_5Cl_2$ for selective CO_2 photoreduction, ACS Catal. 12 (2022) 3965-3973, https://doi.org/10.1021/acscatal.2c00157.
[61] M.R. Ahasan, Y. Wang, R. Wang, In situ DRIFTS and CO-TPD studies of CeO_2 and SiO_2 supported CuO_x catalysts for CO oxidation, Mol. Catal. 518 (2022) 112085, https://doi.org/10.1016/j.mcat.2021.112085.
[62] A.J. Medford, A. Vojvodic, J.S. Hummelshøj, J. Voss, F. Abild-Pedersen, F. Studt, T. Bligaard, A. Nilsson, J.K. Nørskov, From the Sabatier principle to a predictive theory of transition-metal heterogeneous catalysis, J. Catal. 328 (2015) 36–42, https://doi.org/10.1016/j.jcat.2014.12.033.